Advanced Physics Laboratory

Structure Analysis of Powder Samples & Epitaxial Thin Films via X-Ray Diffraction

Name: Manthan Chattopadhyay(3753103), Nicolò De Masi(3746606)

Group: K22

Experiment Date: 30.04.2024

Abstract

This lab explores the nature of X-ray radiation and the diffraction patterns resulting from different materials by the use of $2\theta - \omega$ and ω scans. The samples include two poly-crystalline bulk crystals of Si and ZnO, thin films of ZnO grown on two Sapphire substrates of different orientation, and an unknown powder sample. Analysis of the diffraction patterns and their peaks will give us insight into the structure and orientation of the different crystals as well as the efficacy of the instrumentation used to obtain these results.

Contents

1 Theoretical Background

1.1 Nature of X-rays: Generation & Spectra

X-rays refer to electromagnetic radiations with a wavelength that ranges between $\lambda \approx 10^{-7}m$ and $\lambda \approx 10^{-11}m$, thus making them substantially shorter then visible light and highly energetic. Typical inter atomic distances in crystals range around 0.15–0.4 nm [2], rendering X-rays ideal for diffraction studies. Constructive and destructive interference patterns are expected to become observable when crystalline structures are subjected to X-ray exposure.

In diffraction experiments, an X-ray generator is utilized, typically consisting of either a sealed tube with a fixed target or a more powerful rotating anode system. [3]. Our setup utilizes the former. The vacuum tube, made typically of glass-(ceramic)-metal, functions by emitting electrons from a heated cathode. These electrons are then accelerated by an external voltage U and directed to impact an anode.
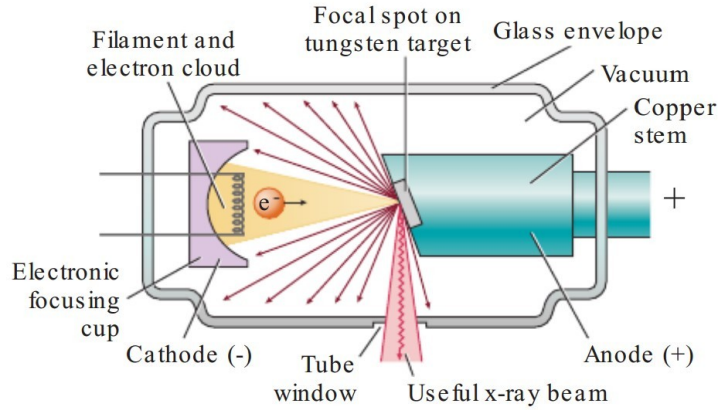
Figure 1: Illustration of a generic x-ray tube

At the anode, electrons are halted and portion of their energy eU is transformed into short-wavelength, high-energy radiation. While the majority of this energy dissipates as heat, approximately 1% is converted into X-rays. Tungsten is used as the anode owing to its high atomic number (Z=74) and melting point (3695K) [7], deeming it a suitable target material for efficient X-ray production.

X-rays are generated through two mechanisms, each resulting in a different spectrum: as a smooth function of the wavelength (*Bremsstrahlung*), and as sharp peaks at specific wavelengths (*Characteristic Peaks*).
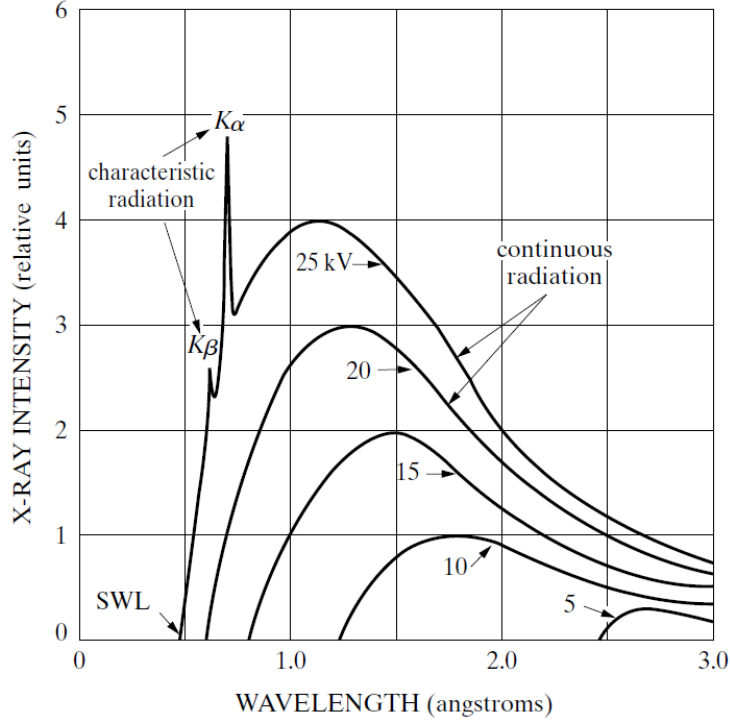
Figure 2: Example X-ray emission spectra of Tungsten at a certain voltage

- *Bremsstrahlung*

  When a charged particle accelerates, it emits radiation as electromagnetic waves. The power of this radiation is described by Larmor's formula:

  $$P = \frac{2}{3} \frac{q^2}{4\pi\epsilon_0 c} \left(\frac{\dot{v}}{c}\right)^2 \tag{1}$$

  The continuous radiation is a result of electrons decelerating upon interaction with the anode material at varying rates. While some electrons may stop abruptly upon a single impact, releasing all their energy instantaneously, others undergo multiple deflections, gradually losing energy through successive interactions with the target atoms. The range of energy emitted thus forms a continuum, but with a maximum energy limit defined by electrons that come to a complete stop during their first collision. This maximum kinetic energy $E_{\text{kin}} = eU$, corresponds the highest frequency of X-ray, ν_{max}, which can be emitted. As a result, the wavelength of this maximum energy radiation has a lower limit [3], given by:

  $$\lambda \geq \lambda_{min} = \frac{hc}{eV} \tag{2}$$

  Note that even though the intensity of the Bremsstrahlung can be amplified by using heavy elements at the anode, or increasing current, the short-wavelength limit and wavelength distribution are functions of only the voltage.

- *Characteristic Peaks*

  On the other hand, the sharp peaks are present due to the excitation of electrons of the anode material by the high-energy free flowing electrons of the cathode. The excited electrons will fill higher energy shells thus creating vacancies in the inner shells. Electrons from higher shells occupy the vacancies and the energy released in this process is emitted as X-ray radiation of specific wavelength depending on the specific transitions. This produces the characteristic peaks we superimpose to the continuous spectra. Each peak, or "line" is the result of jumps between different orbital positions. Note that these lines will only appear above a voltage threshold, as they will otherwise be absorbed into the Bremsstrahlung. We will discuss the different characteristic lines in the next section.

1.2 Characteristic X-ray lines: Siegbahn notation

Characteristic X-ray lines are distinctively named based on the metal used to generate them. These lines are categorized into various groups, and the nomenclature developed for their identification is outlined below: [4]:

K	Transition of an electron to the K shell (n=1)
L	Transition of an electron to the L shell (n=2)
M	Transition of an electron to the M shell (n=3)

In the context of x-ray diffraction, only the K lines tend to be useful, as the L and M lines, which present longer-wavelengths, are too easily absorbed in the continuous spectrum.

We can further split the K line grouping in the following way:

K_α	K-shell vacancy filled by an electron from the L shell
K_β	K-shell vacancy filled by an electron from the M shell

It is easier for an electron from the L shell to fill K-shell vacancies, as such K_α lines will appear substantially more intensely then K_β.
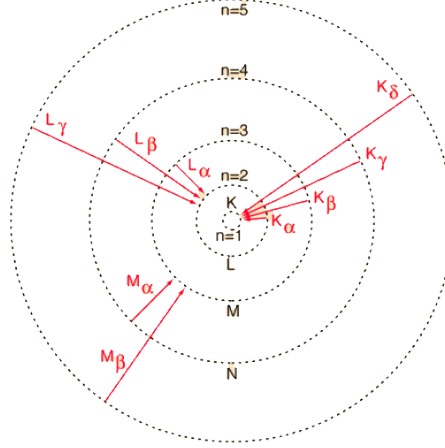
Figure 3: Characteristic X-ray Transitions

Due to fine structure (spin-orbit coupling), the K_α transitions are further categorized into two spectral lines: K_{α_1} and K_{α_2}. The K_{α_1} line corresponds to the transition $2\,^2P_{1/2} \rightarrow 1\,^2S_{1/2}$ while the K_{α_2} line corresponds to $2\,^2P_{3/2} \rightarrow 1\,^2S_{1/2}$, owing to the selection rules for optical transitions, $\Delta l = \pm 1$ and $\Delta j = 0, \pm 1$.

The K_{α_1} emission has a slightly lower wavelength than the K_{α_2} emission, but the difference is so small that they are often not resolved apart as a *doublet* but considered as a single K_α single line. For all elements, the ratio of the intensities of K_{α_1} and K_{α_2} is very close to 2:1 [5]. The same can be said for $K_{\beta_{1,2}}$, but they are even harder to resolve and fundamentally beyond the scope of X-ray diffraction. Since the $2\,^2P_{3/2}$ state has four m_j values $(-3/2, 3/2, 1/2, -1/2)$, compared to the two from $2\,^2P_{1/2}$ $(-1/2, 1/2)$, it is statistically more populated causing the aforementioned intensity ratio. In the context of our experiment, only $K_{\alpha_{1,2}}$ and K_β will be treated. For tungsten, the values are the following [6]:

	Energies of X-ray emission lines (keV)	Associated wavelength (Å)
K_{α_1}	59318.24	0.209
K_{α_2}	57981.7	0.213
K_β	67244.3	0.184

1.3 Absorption of X-rays

When X-rays interact with any material, they are partially transmitted and partially absorbed. Röntgen established that the fractional reduction in the intensity I of an X-ray beam, as it penetrates a homogeneous substance, is directly proportional to the path length x traversed by the beam [4]:

$$-\frac{dI}{I} = \mu dx \tag{3}$$

where the proportionality constant μ is called the linear absorption coefficient, which is proportional to the density ρ of the substance, and also a function of

the wavelength of the x-rays. Integrating (3) yields,

$$I_x = I_0 e^{-(\mu/\rho)\rho x} \tag{4}$$

The modified quantity μ/ρ is called the mass absorption coefficient which is a constant of the material and independent of the substance's physical state. Variation of the mass absorption coefficient with respect to wavelength gives us insight into how the X-rays interact with the material. A typical plot of μ/ρ against wavelength reveals distinctive patterns referred to as branches, which are interspersed with sharp discontinuities (Figure 6). These discontinuities primarily arise not from scattering (which would imply a random loss of intensity), but from true absorption due to electronic transitions within the atoms. Analogous to the interaction of an energetic electron with an atom, an X-ray quantum with sufficient energy can liberate an inner-shell electron. In this process, the incoming X-ray's energy is converted into kinetic energy of the ejected photo-electron and fluorescent radiation that is emitted as an electron relaxes back from a higher energy level to a lower one.
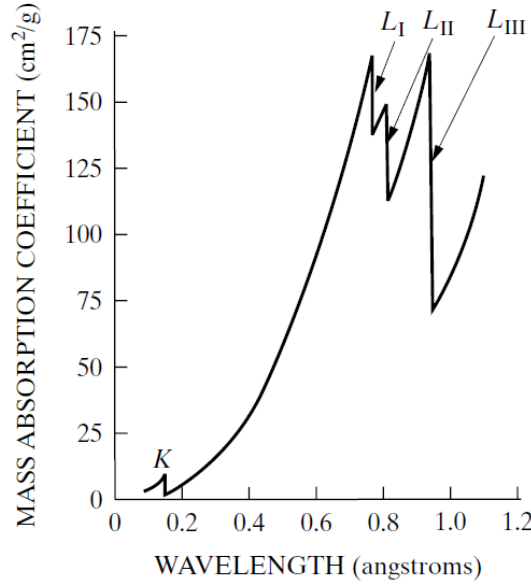
Figure 4: Absorption coefficient of lead, with K and L absorption edges [4]

As the frequency is increased, a new threshold value required to create an electron vacancy is reached. The secondary peaks are owed again to fine structure of the element. Absorption of an X-ray quantum however, does not always result in the production of K-shell radiation. The absorbed energy may also be released through the ejection of an outer-shell electron possessing the exact kinetic energy equivalent to the absorbed quantum, thus creating an ionisation. This process is referred to as the Auger effect and particularly seen in lighter atoms (Z<31).

1.4 Filtering of X-rays

Diffraction experiments necessitate radiation that is as monochromatic as possible. However, when an X-ray tube is operated above a certain voltage, the emitted beam comprises not only the intense K_α line but also the weaker K_β line and a continuous spectrum as seen in Figure 2. The relative intensity of these undesirable components can be reduced by filtering the beam with a material whose K absorption edge is lies between the wavelengths of the K_α and K_β lines of the target metal. For anode metals with atomic numbers around 30, the filter metal will typically have an atomic number that is one less than the anode metal. An example filtration of copper radiation (Z=29) via a nickel (Z=28) filter is shown below:
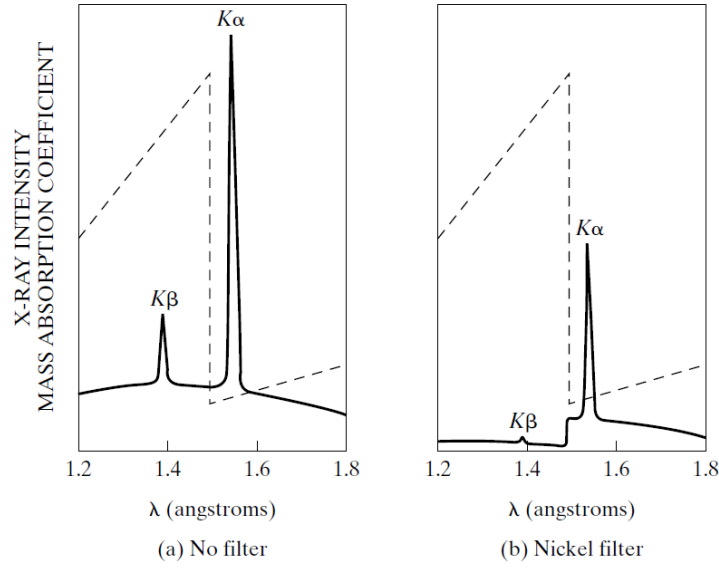
Figure 5: Spectra of copper radiation (a) before and (b) after passage through nickel filter. The dashed line denotes mass absorption coefficient of nickel. [4]

The effectiveness of filtration increases with the thickness of the filter, resulting in a lower ratio of K_β to K_α intensity. However, perfect filtration is unattainable and we compromise between lower suppression of K_β intensity and accidental weakening of K_α. In practice, reducing K_α by half of its original value typically lowers K_β to K_α intensity ratio from 1/9 in incident beam to about 1/500 in transmitted beam which is sufficiently low.

1.5 Crystal Systems: Direct & Reciprocal Lattice

The fundamental concept behind any crystalline solid is the direct lattice, which specifies the periodic array in which the repeated units of the crystal are arranged. Atomic positions within a crystal are defined as fractions of lattice translations,

$$\mathbf{R} = n_1\mathbf{a_1} + n_2\mathbf{a_2} + n_3\mathbf{a_3} \tag{5}$$

where $\mathbf{a_1}, \mathbf{a_2}$ and $\mathbf{a_3}$ are any three vectors not all in the same plane, and n_1, n_2 and n_3 range through all integral values. The vectors $\mathbf{a_i}$ are called primitive vectors that span the so called direct lattice. For atoms within the unit cell, $0 \le \mathbf{a_i} < 1$.
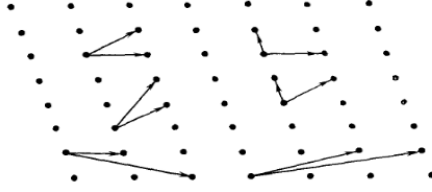

Figure 6: Examples of primitive vectors for a 2D lattice [8]

We now require a tool that helps us relate angular information obtained from diffraction experiments, with the direct lattice. This motivates the formulation of the reciprocal lattice: The set of all wave vectors $\mathbf{K}$ that yield plane waves with the periodicity of a given direct lattice is known as reciprocal lattice [9]. Analytically, given a direct lattice vector $\mathbf{R}$,

$$e^{i\mathbf{K}\cdot(\mathbf{r}+\mathbf{R})} = e^{i\mathbf{K}\cdot\mathbf{r}} \tag{6}$$

holds for any $\mathbf{r}$. Factoring the above equation, we can state that the reciprocal lattice is a set of wave vectors $\mathbf{K}$ satisfying

$$e^{i\mathbf{K}\cdot\mathbf{R}} = 1 \tag{7}$$

Each primitive vector of the reciprocal lattice can be generated by

$$\mathbf{b_i} = 2\pi \frac{\mathbf{a_j} \times \mathbf{a_k}}{\mathbf{a_i} \cdot (\mathbf{a_j} \times \mathbf{a_k})} \tag{8}$$

Note that the reciprocal lattice conserves the underlying symmetry of the direct lattice. In group theory terms, the point group of the reciprocal lattice is the same as the point group of the direct lattice.

1.6 Miller Indices & Lattice Planes

The vectors of reciprocal lattice and planes of points in direct lattice are geometrically related. This relation is imperative in understanding the role the reciprocal lattice plays in theory of diffraction.

For a given direct lattice, a *lattice plane* is defined to be any plane containing at least three noncollinear lattice points. Due to translational symmetry, any such

plane will contain infinitely many lattice points, which will themselves form a 2D lattice. A *family of lattice planes* is a set of parallel, equally spaced lattice planes which together contain points of the 3D lattice. The geometric relation between lattice planes and reciprocal lattice is given by the theorem below [9]:

> For any family of lattice planes separated by a distance d, there are reciprocal lattice vectors perpendicular to the planes, the shortest of which have a length of $2\pi/d$. Conversely, for any reciprocal vector $\mathbf{K}$, there is a family of lattice planes normal to $\mathbf{K}$, and separated by a distance d, where $2\pi/d$ is the length of the shortest reciprocal lattice vector parallel to $\mathbf{K}$.

Generally, we describe the orientation of a plane by stating a vector normal to it. It is now convenient to use the shortest reciprocal lattice vector as a unique choice of representing vector normal to a lattice plane. We thus define the *Miller Indices* of a plane as the coordinates of the shortest reciprocal lattice vector normal to that plane, with respect to a specified set of primitive reciprocal lattice vectors. A plane with miller indices h, k, l will be normal to the reciprocal lattice vector $h\mathbf{b_1} + k\mathbf{b_2} + l\mathbf{b_3}$.
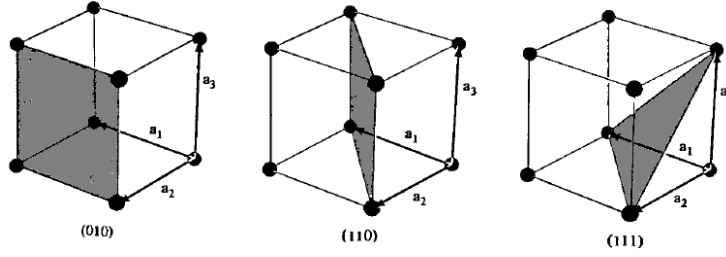

Figure 7: Lattice planes and their Miller indices in a simple cubic lattice [9]

In practice, it is only when we study noncubic crystals that we must remember that Miller indices are coordinates in the reciprocal system, and not the direct lattice (reciprocal lattice of simple cubic is also simple cubic, but with a length change of $2\pi/a$).

Due to the definition of $\mathbf{K}$ in (7), crystallographers also define Miller indices to be a set of integers with no common factors, inversely proportional to the intercepts of the plane along the axes:
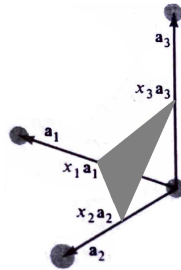

Figure 8: Crystallographic definition of Miller indices [9]

11

Thus, $h : k : l = \frac{1}{x_1} : \frac{1}{x_2} : \frac{1}{x_3}$ where for a non-intersecting axis $\mathbf{a_i}$, $x_i \to \infty$ and corresponding index will be 0.

1.7 Bragg's Equation

We have covered both the structural geometry of crystals and the nature of X-rays. Typical interatomic distances in a solid are on the order of an angstrom (10^{-10}m). To probe these distances effectively, electromagnetic radiation with energy on the order of keV is required, which are characteristic X-ray energies. Bragg's law provides a description of the interaction between X-ray waves and the crystal lattice. In crystals, for certain wavelengths and incident directions, intense peaks of scattered radiation (Bragg peaks) were observed.

Bragg explained this phenomenon by considering a crystal as consisting of parallel planes of atoms (lattice planes), separated by a distance d. The condition for a sharp peak in the scattered radiation were: (1) specular reflection of X-rays (angle of incidence equals angle of reflection) and (2) rays reflected off of successive lattice planes interfere constructively.

The following figure illustrates this phenomena on a crystal with multiple atoms (P, K ...) arranged together in parallel lattice planes (A,B,C).

Figure 9: Bragg reflection from a family of lattice planes [4]

The X-ray beam is ideally monochromatic with wavelength λ, and uniquely incident with angle θ. For ease of illustration we split it into different rays, each interacting with a different lattice plane, but maintaining the same angle of incidence. The Bragg assumption of specular reflection is equivalent to the assumption that rays scattered from individual atoms in the *same plane* interfere constructively [9]. This can be geometrically proven, by noting the path difference between **1** and **1a**. We see that their path difference consists of the segment lengths QK and PR, both of which can be expressed as $PK cos\theta$. This can be extended to all point scaterrers within the same plane, justifying Bragg's assumption of specular reflection.

We now consider ray **1** and ray **2**. Ray **2** travels an additional path length of $ML + LN$ relative to **1**. Based on the geometry of the system, $ML + LN = d' sin\theta + d' sin\theta = 2d' sin\theta$, where d' represents the distance between parallel lattice planes. This holds true for all parallel rays reflected off of adjoining lattice planes.

Constructive interference takes place when the path difference between two rays is equal to 0 or any whole number of wavelengths. With n being the order of diffraction, we write Bragg's law as:

$$n\lambda = 2d' sin\theta \tag{9}$$

Bragg's law itself also gives us an explanation of why X-rays are used to observe crystal structures. Given that $sin\theta$ is a periodic function, it follows from (9) that:

$$n\lambda < 2d' \tag{10}$$

For $n = 1$ and the average $d' \approx 3$ Å in crystal structure, it follows that the maximum wavelength we can study crystals with is $\lambda \approx 6$ Å.

1.8 Von Laue Approach: Diffraction & Reciprocal Lattice

The sectioning of a crystal into planes is not a unique choice. The same portion of lattice shown in Figure 9, can also be sectioned as:
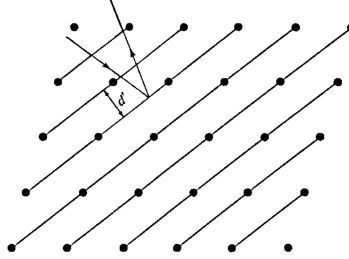
Figure 10: Different sectioning of lattice planes [9]

Without imposing *ad hoc* assumptions of specualr reflection, we regard the crystal to be composed of point scatterers, located at each lattice site $\mathbf{R}$. The condition of constructive interference can be derived by first considering two scatterers, seperated by a displacement vector $\mathbf{d}$ as shown in Figure 11
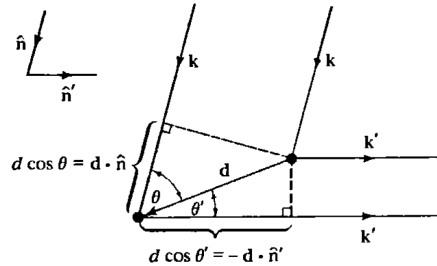
Figure 11: Path difference of rays scattered by two lattice points separated by $\mathbf{d}$ [9]

Suppose incident X-ray along the direction $\hat{\mathbf{n}}$ with wave vector $\mathbf{k} = 2\pi\hat{\mathbf{n}}/\lambda$ is scattered at two lattice sites, and observed along the $\hat{\mathbf{n}}'$ direction. To a good

approximation, we assume that the bulk of the scattered radiation is elastically scattered (i.e. no change in wavelength). The observed ray will have wave vector $\mathbf{k}' = 2\pi\hat{\mathbf{n}}'/\lambda$, provided that the path difference between them is an integral number of the wavelength. From Figure 11 it can be seen that this path difference is,

$$d\cos\theta + d\cos\theta' = \mathbf{d} \cdot (\hat{\mathbf{n}} - \hat{\mathbf{n}}') \tag{11}$$

For constructive interference,

$$\begin{aligned} \mathbf{d} \cdot (\hat{\mathbf{n}} - \hat{\mathbf{n}}') &= m\lambda \\ \implies \mathbf{d} \cdot (\mathbf{k} - \mathbf{k}') &= 2\pi m \end{aligned} \tag{12}$$

for an integral m. If we now consider not just two, but all point scatterers of the lattice, condition (12) should hold for all direct lattice vectors such that,

$$\mathbf{R} \cdot (\mathbf{k} - \mathbf{k}') = 2\pi m \tag{13}$$

for all $\mathbf{R} \in$ Direct Lattice. An equivalent formulation of (13) is realised to link it with the definition of reciprocal lattice (7) such that,

$$e^{i(\mathbf{k}' - \mathbf{k}) \cdot \mathbf{R}} = 1 \tag{14}$$

Thus according to the Laue condition, constructive interference occurs whenever the change in wave vector $\mathbf{K} = \mathbf{k}' - \mathbf{k}$, is a vector of the reciprocal lattice. An equivalence principle between Bragg and von Laue formulation must be taken into account:

> A Laue diffraction peak corresponding to a change in wave vector given by reciprocal lattice vector $\mathbf{K}$ corresponds to a Bragg reflection from the family of lattice planes perpendicular to $\mathbf{K}$. The order n of the Bragg reflection is magnitude of $\mathbf{K}$ divided by the shortest reciprocal lattice vector parallel to $\mathbf{K}$ [9].

In practice, one will most probably not see any Bragg peaks for a fixed incident $\mathbf{k}$ as the tip of the wave vector will not lie on a $k-$space Bragg plane. We will thus have to relax the constraint of fixed $\mathbf{k}$, either by varying the wavelength, or the orientation of the sample with respect to incident beam.

1.9   Planar Spacing of the 7 Crystal Systems

As seen in Section 1.6, miller indices describe the orientation of a crystal plane in a lattice. They are inversely proportional to the intercepts that the plane makes with the crystallographic axes a, b, and c, which are normalized by the unit cell dimensions along these axes. The distance d_{hkl} between adjacent planes, associated with the Miller indices $h, k,$ and l can be calculated using:

$$d_{hkl} = \frac{1}{\sqrt{\frac{h^2}{a^2} + \frac{k^2}{b^2} + \frac{l^2}{c^2}}} \tag{15}$$

where we have assumed a cubic crystal with unequal, orthogonal axes. Similar equations can be evaluated for each of the 7 crystal systems, taking into account their respective symmetries as seen in appendix A.

1.10 Penetration Depth of X-Rays

X-rays incident on our samples are reflected, transmitted, and also absorbed as shown in section 1.3. It is important that we have an estimation of penetration depth of our incident ray, so we can use samples of appropriate dimensions. The absorption fraction $A(x)$ is expressed via the linear absorption coefficient μ as seen in equation (4) and has the form

$$A(x) = 1 - \exp\left\{-\mu x \left(\frac{1}{\sin\omega} + \frac{1}{\sin 2\theta - \omega}\right)\right\} \tag{16}$$

where x is a distance in the material along the incident beam, θ the diffraction angle, and ω the angle of incidence [10].

The penetration depth d is defined as the x value where the intensity of the beam inside the material has decayed to $1/e \approx 37\%$ of the original, and is given by

$$d = \left(\frac{\mu}{\sin\omega} + \frac{\mu}{\sin 2\theta - \omega}\right)^{-1} \tag{17}$$

Experimental values of penetration depth of various elements subjected to cobalt, copper, and molybdenum radiation are shown below:

	Z	ϱ [gcm^{-3}]	Co-Strahlung $\omega = 1°$	$\omega = 15°$	Cu-Strahlung $\omega = 1°$	$\omega = 15°$	Mo-Strahlung $\omega = 1°$	$\omega = 15°$
C	6	2,27	9,64	17,37	15,35	117,9	169,2	1 300
Al	13	2,70	0,83	6,38	1,29	9,91	12,70	97,9
Si	14	2,33	0,77	5,95	1,20	9,23	11,75	90,3
Fe	26	7,86	0,38	2,89	0,067	0,52	0,58	4,49
Cu	29	8,92	0,24	1,88	0,37	2,82	0,39	2,98
Zn	30	7,14	0,28	2,13	0,42	3,21	0,45	3,43
Zr	40	6,51	0,12	0,99	0,19	1,48	1,60	12,31
W	74	19,25	0,035	0,27	0,052	0,40	0,092	0,70

Figure 12: Penetration depth(μ) of different elements subjected to three types of radiation, with varying angle of incidence [10]

When performing X-ray diffraction of heteroepitaxial thin films, we must use radiation with sufficient penetration depth such that we get interference pattern from both thin film and substrate.

1.11 Structure of Polycrystalline Samples & Heteroepitaxial Thin Films

In regards to the orientation of grains of crystals, three distinct structures are commonly recognized: monocrystalline, polycrystalline, and amorphous materials. Monocrystalline materials consist of crystal lattices free from any defects or impurities. Amorphous materials, in contrast, only exhibit short-range order. Polycrystalline materials are composed of multiple grains of varying sizes and orientations, each with a perfect crystal structure. This structure is prevalent in most metals and is commonly observed in nature due to the frequent

occurrence of defects in solids. The first part of this report will deal with a polycrystalline bulk sample of ZnO.
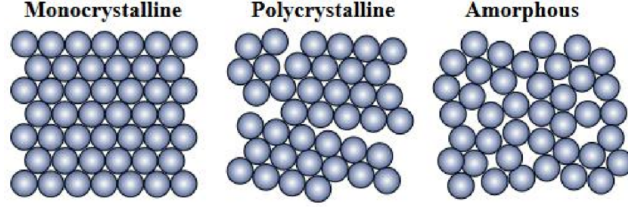

Figure 13: Overview of different grain structures of crystals [11]

The second part of this report will be concerned with diffraction from a heteroepitaxial thin film (i.e. thin film and substrate are of different materials) of ZnO grown on sapphire substrate. A lattice mismatch fraction is given by

$$\frac{\Delta a}{a} = \frac{a_{sub} - a_{film}}{a_{sub}} \tag{18}$$

where a_{sub} and a_{film} are the relaxed lattice constants [13].
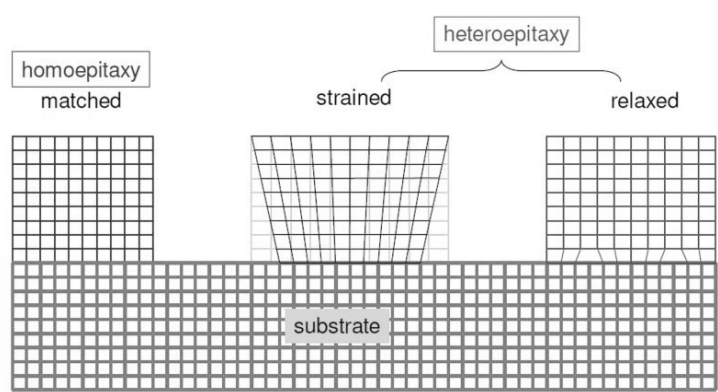
Figure 14: Epitaxial film growth modes [12]

In the case of minor lattice mismatches, an epitaxial film can undergo pseudo-morphic growth, conforming to the substrate's in-plane lattice constant and accumulating biaxial strain [13]. Dislocations within this context are categorized into two types: screw-type and edge-type, via the use of a so called Burgers vector that quantifies the magnitude and direction of the distortion. It aligns with the dislocation line in screw-type, while it is perpendicular in edge-type dislocations.
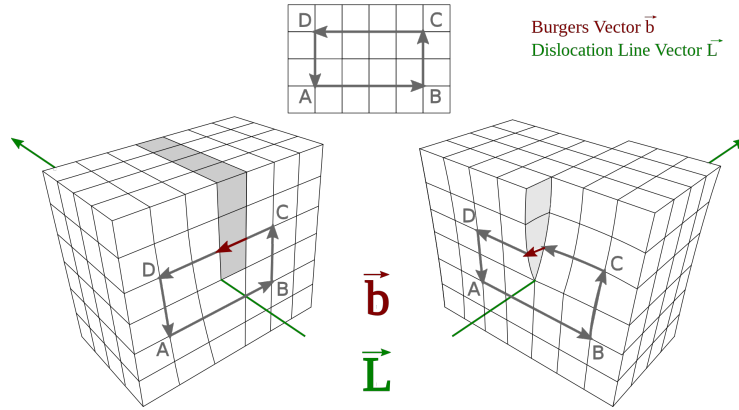
Figure 15: Burgers vector in edge dislocation (left) & screw dislocation (right) [14]

Dislocations naturally organize into the most stable configurations as it provides thermodynamic stability; edge-type dislocations tend to cluster. Such clusters are known as grain boundaries and represent two-dimensional defects and delineate the border between two monocrystalline areas, or crystallites, that are rotated relative to each other. Edge-type dislocations generally induce a twist in the crystallites, whereas screw-type dislocations may lead to a tilt. In later sections, we will discuss the spread of crystal plane orientations (also known as mosaicity) among the crystallites, as their misalignment isn't random but tends to fall within a small angular distribution.

2 Experimental Setup

2.1 Diffractometer & Scan Types

This lab is performed with the Philips X'Pert diffractometer in Bragg-Brentano geometry. An overview of a typical diffractometer is depicted below:
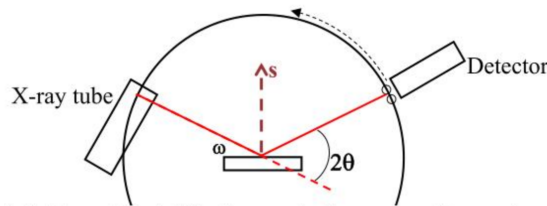
Figure 16: Schematic of a typical diffractometer undergoing detector scan [15]

We define an incident angle ω between the sample and X-ray source. The diffracted angle 2θ is defined between incident and detection angle. The automated scanning software has the ability to perform three types of scans:

- **Detector Scan**: Plots X-ray intensity vs. 2θ without varying ω.

- **Coupled Scan**: Plots X-ray intensity vs. 2θ, but ω also changes that is linked to 2θ such that $\omega = \frac{1}{2}2\theta+$offset. Importantly, the detector moves at twice the angular rate of the source.

17

- **Rocking Curve**: Plots X-ray intensity vs. ω by fixing the detector at the center of a Bragg peak and tilting the sample within a provided range.

The source and detector are mounted on a goniometer that can rotate them around the sample.

2.2 Errors in Goniometer Measurement & Methods for Error Elimination

Determining lattice parameters of our sample requires accurate measurement of the angle θ, which then facilitates the calculation of the interplanar spacing (d) and the Miller indices. However in Bragg's law, $sin\theta$ is required instead of θ. The trigonometric function behaves such that, as θ approaches 90° (or 2θ approaches 180°), the smaller the relative error tends to be as depicted in Figure 17.
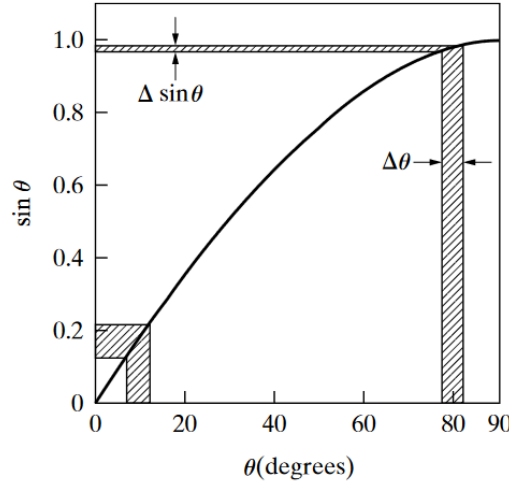
Figure 17: Difference in relative value of $sin\theta$ with respect to θ between 0 and 90 degrees [4]

For $2\theta - \omega$ scans, with a fixed step length of 0.02° we can assume a consistent error in θ, thereby dealing with a variable error for the derived sin function and subsequent calculations that approaches 0 as θ approaches 90°.

This can be minimized by the use of extrapolation functions, with a slope of the extrapolation line proportional to the magnitudes of the errors. [16]. The magnitude of errors, and therefore the choice of extrapolation function, depends on the various types of errors incurred when using a diffractometer. [4]. The main ones we need to be aware of are:

- Use of a flat sample instead of a curved one in order to conform to the moving beam.

- Absorption in the sample

These sources cause proportionality of $\frac{\Delta d}{d}$ to $cos^2\theta$:

$$\frac{\Delta d}{d} = \frac{\Delta a}{a_0} = \frac{a - a_0}{a_0} = k_1 cos^2\theta \qquad (19)$$
$$\implies a = a_0 + a_0 k_1 cos^2\theta$$

Where $a_0 \to a$ for $\theta \to 90$ and k_1 is a constant

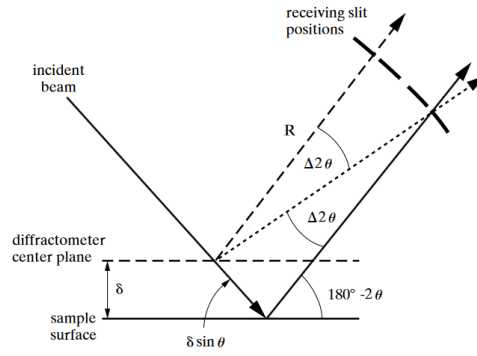- Displacement of the sample from the central axis of the diffractometer (fig. 18.

Figure 18: Displaced sample reflective surfaces in a diffractometer set up [4]

This causes an error in d given by: $\frac{\Delta d}{d} = \frac{k_2 cos^2\theta}{sin\theta}$. It follows similar to (19) that our extrapolation function will be:

$$a = a_o + a_o k_2 \frac{cos^2\theta}{sin\theta} \qquad (20)$$

- Error due to the vertical divergence of the incident beam.

This effect is minimized by the **Nelson-Riley function**: $\left[\frac{cos^2\theta}{sin\theta} + \frac{cos^2\theta}{\theta}\right]$ (Nelson-Riley function), which results in:

$$a = a_o + a_o k_3 \left(\frac{cos^2\theta}{sin\theta} + \frac{cos^2\theta}{\theta}\right) \qquad (21)$$

The lattice parameters derived using different Bragg peaks will be plotted against the discussed error functions.

3 Results & Discussion

3.1 Task 1

In this first task we measure the diffraction patterns of two polycrystalline bulk samples with $2\theta - \omega$ scans.

3.1.1 Silicon

We analyze our silicon sample in a $20° \leq 2\theta \leq 140°$ range. We use a step size of $0.02°$ and measurement rate of 0.5 seconds per step. The diffraction spectra is depicted below:
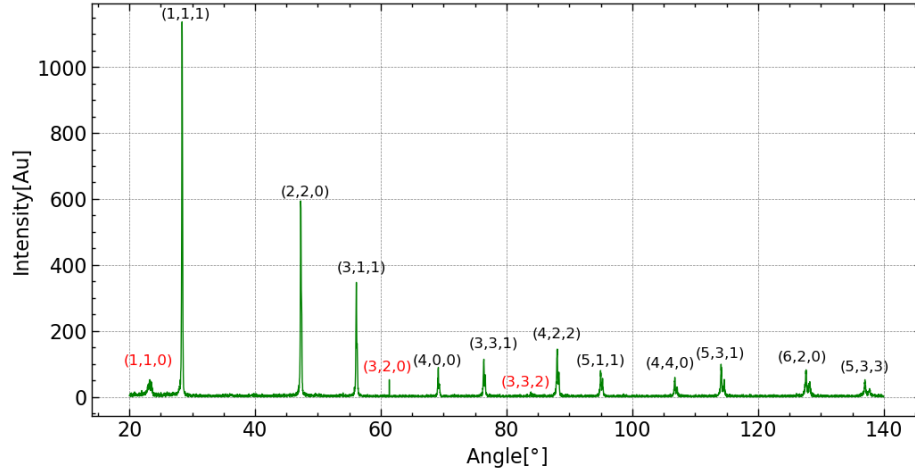
Figure 19: Diffraction pattern of a Silicon sample with associated Miller indices. Peaks marked in red were calculated manually.

Figure 19 shows the obtained Bragg peaks and their associated Miller indices. These were obtained by scanning and finding the best fitting material in the the PC-PDF data base. The best match was pure a silicon sample with reference code 00-005-0565. There was good accordance between all peaks with identical scan range, but three of the least intense peaks found no match. For these we associated the appropriate Miller indices using equation (22), appropriate d-spacing as given in Table 1 and the appropriate lattice parameter a, which will be discussed in the next section.

Additionally, a $K_{\alpha_1}/K_{\alpha_2}$ deconvolution was performed using the in-built feature in HighScore with the precise values of the deconvoluted peaks presented in the table below:

hlk	Position (K_{α_1})[°]	FWHM [°]	d-spacing [Å]	Rel. Int.[%]	Ass. K_{α_2} pos.[°]
(110)	23,2426	0,8677	3,82393	5,00	23,3011
(111)	28,3935	0,1184	3,14085	100,00	28,4655
(220)	47,2714	0,1232	1,92133	53,87	47,3960
(311)	56,1049	0,1287	1,63796	29,68	56,2567
*(320)**	63.3600	—	1,50997	4.75	—
(400)	69,1312	0,1299	1,35772	7,64	69,3275
(331)	76,3774	0,1510	1,24593	10,42	76,6016
(332)	84,0828	3,0740	1,15027	0,16	84,3398
(422)	88,0484	0,1623	1,10840	13,12	88,3239
(511)	94,9721	0,1917	1,04502	6,69	95,2831
(440)	106,7558	0,1952	0,95977	4,86	107,1398
(531)	114,1427	0,2171	0,91773	7,78	114,5836
(620)	127,6279	0,2995	0,85840	6,47	128,2099
(533)	136,9977	0,3583	0,82791	3,40	137,7264

[*] the peak detected at $2\theta = 63.36$ °, which we assigned to (3,2,0) has such a low resolution (FWHM=0 with step lenght of 0.02 °) that the software doesn't recognise it as one.

Table 1: Position, FWHM, d-spacing and relative intensity for all Si peaks, found using the X'Pert High Score software.

Crystal structure of Silicon and lattice parameters

Silicon is a Face Centered Cubic structure (FCC), with the lattice parameters being $a = b = c$ and $\alpha = \beta = \gamma = 90$. For this reason eq. (15) can be rewritten as the one in Appendix A for cubic unit cell:

$$\frac{1}{d_{hkl}^2} = \frac{h^2 + k^2 + l^2}{a^2} \tag{22}$$

Silicon crystallises in the so-called **diamond cubic structure**, which consists of two interpenetrating FCC lattices, with a $a/4$ offset along each axis. Thus, the lattice basis is two silicon atoms.
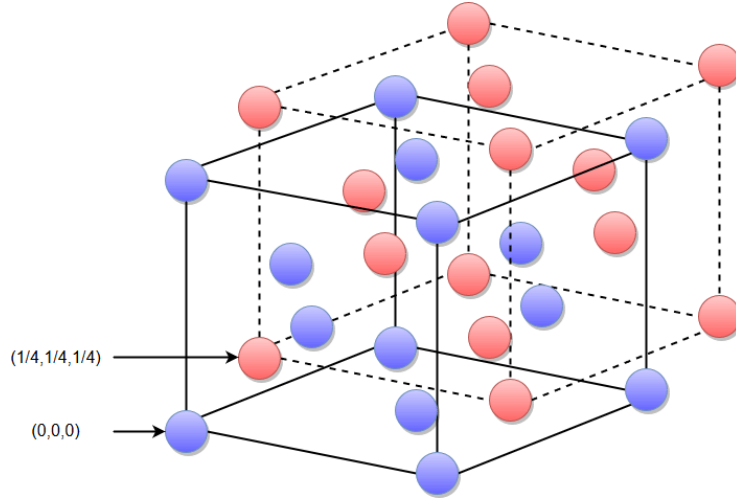
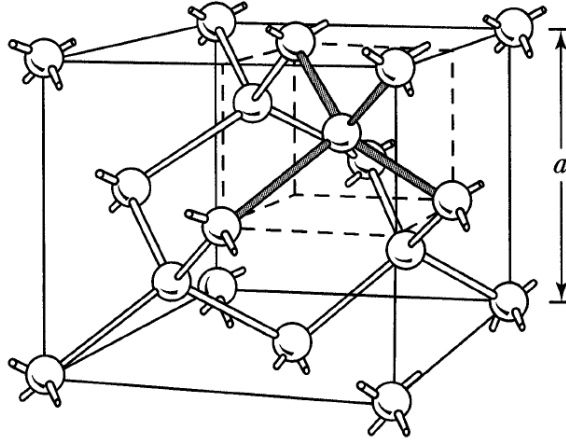Figure 20: Unit cell of Silicon interpreted as interpenetrating fcc lattices [17]

Figure 21: Silicon Diamond Structure [9]

Our matching sample gives a lattice parameter $a = 5.4301$ Å. Rewriting equation 22 in relationship to Bragg's law we can estimate a for all (h, l, k) and compare:

$$a = \frac{\lambda \sqrt{h^2 + k^2 + l^2}}{2 sin\theta} \tag{23}$$

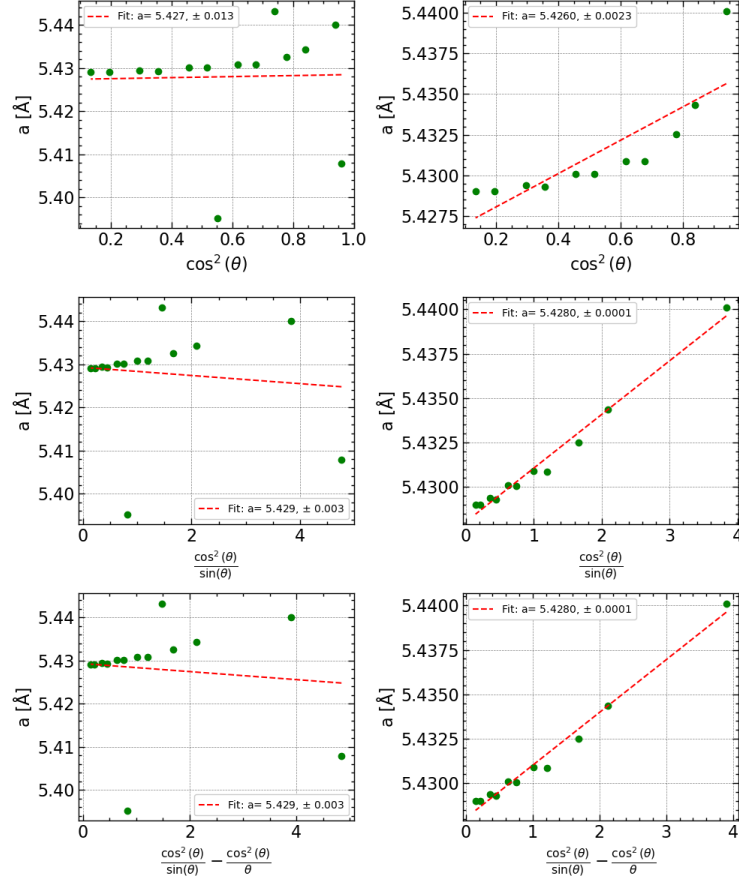To minimize errors, we fit our a values to the extrapolation functions we discussed in Section 2.2. Specifically we use equations (19), (20) and (21).

Figure 22: Different Extrapolation function corrections with (left) and without (right) additionally indexed miller planes

We observe that the peaks we indexed manually, return values of a that are relatively less close to the theory. Their contribution to every extrapolation function fit however, brought our calculated lattice constant closer to theoretical value. For Silicon with $a = 5.431$ Å, the graphs on the left side served as a better approximation.

Regarding the behaviour of the extrapolation functions, we see that the closest values to the theoretical is obtained with the use of the Nelson-Riley function and with $cos^2\theta/sin\theta$, indicating that predominant errors in our set-up are displacements of our samples from the central axis of the diffractometer and the vertical divergence of the incident beam.

3.1.2 Zinc Oxide
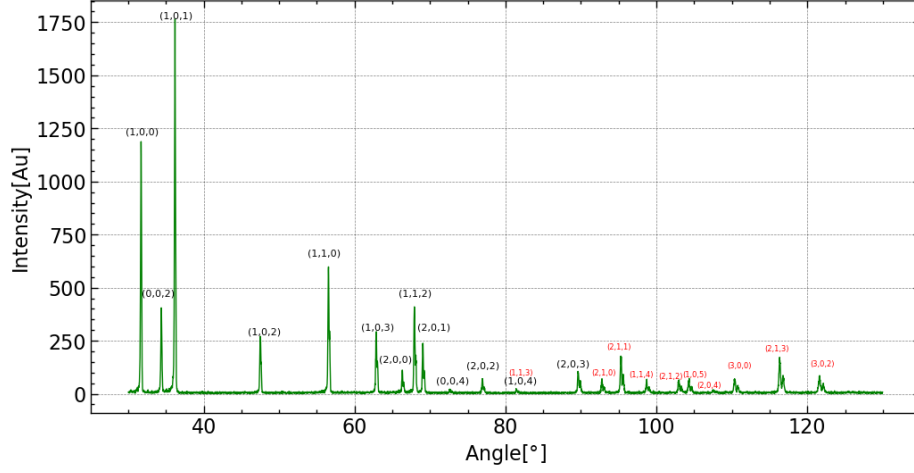
Figure 23: Diffraction pattern of a powdered ZnO sample with associated Miller indices. Peaks marked in red were calculated manually.

The Bragg peaks and their associated Miller indices were obtained analogously to Silicon. The best match was a ZnO sample with reference code 01-075-0576. There was good accordance between all peaks within the reference's scan range, however it only ranged till $2\theta = 90°$. The remaining peaks were indexed manually analogously to Silicon, along with a $K_{\alpha_1}/K_{\alpha_2}$ deconvolution, presented below:

hlk	Position (K_{α_1})[°]	FWHM [°]	d-spacing [Å]	Rel. Int.[%]	Ass. K_{α_2} pos.[°]
(100)	31.6797	0.1129	2.82213	66.72	31.7605
(002)	34.3691	0.1169	2.60720	22.34	34.4572
(101)	36.1780	0.1104	2.48088	100.00	36.2710
(102)	47.4884	0.1169	1.91306	17.03	47.6136
(110)	56.5269	0.1285	1.62673	35.16	56.6800
(103)	62.8563	0.1323	1.47729	17.84	63.0303
(200)	66.3182	0.1297	1.40831	6.14	66.5043
(112)	67.9194	0.1359	1.37896	24.22	68.1112
(201)	69.0408	0.1285	1.35927	14.32	69.2367
(004)	72.6179	0.4528	1.30087	0.61	72.8273
(202)	76.9357	0.1474	1.23827	3.86	77.1621
(104) *113* *	81.4466	0.1843	1.18070	0.88	81.6919
(203)	89.6313	0.1723	1.09289	6.10	89.9145
(210)	92.7691	0.1764	1.06397	3.22	93.0684
(211)	95.2945	0.1785	1.04234	9.99	95.6073
(114)	98.7037	0.1809	1.01526	3.13	99.0359
(212)	102.956	0.1971	0.98457	3.60	103.314
(105)	104.285	0.2014	0.97563	3.55	104.652
(204)	107.531	0.2218	0.95499	0.70	107.920
(300)	110.376	0.2308	0.93821	3.86	110.786
(213)	116.340	0.2332	0.90664	9.60	116.800
(302)	121.617	0.2690	0.88237	4.55	122.128

* At $2\theta \approx 81.45°$ we are able to manually index a second reflection plane which gives very similar d-spacing (1,1,3).

Table 2: Position, FWHM, d-spacing and relative intensity for all ZnO peaks, found using the X'Pert High Score software and by manual indexing

Crystal structure of ZnO and lattice parameters

ZnO like a lot of group II-VI binary compound semiconductors crystallizes in in either cubic, zinc blende or hexagonal wurtzite structure, where each anion is surrounded by four cations at the corners of a tetrahedron. In ambient conditions, the thermodynamically stable phase is wurtzite. The diatomic basis is depicted below:
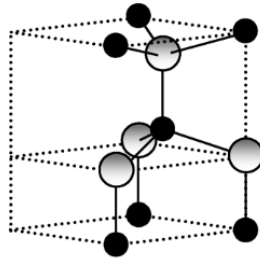

Figure 24: Diatomic basis of hexagonal Wurtzite structure. Shaded gray and black spheres denote Zn and O atoms, respectively [18]

The unit cells form a stacked hexagonal Wurtzite structure where four Miller indices are necessary to distinguish similar planes rotated by 120°.
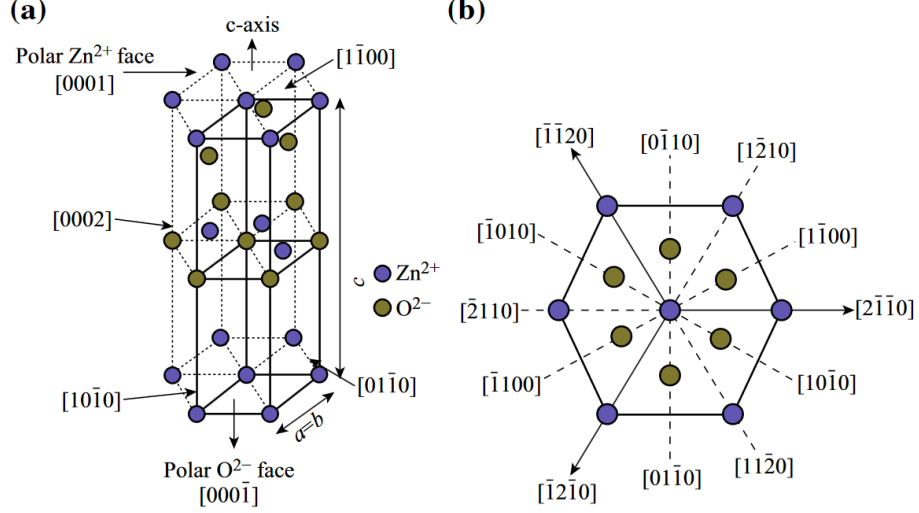

Figure 25: (a) ZnO unit cell with wurtzite structure. (b) Various crystal planes of ZnO Wurtzite structure [19]

For a hexagonal unit cell:

$$\frac{1}{d_{hkl}^2} = \frac{4}{3}\left(\frac{h^2 + k^2 + hk}{a^2}\right) + \frac{l^2}{c^2} \tag{24}$$

If we express d_{hlk} through Bragg's law, we get (considering first order refraction):

$$\frac{4sin^2\theta}{\lambda^2} = \frac{4}{3}\left(\frac{h^2 + k^2 + hk}{a^2}\right) + \frac{l^2}{c^2} \tag{25}$$

From 25, if we set $l = 0$ (thus only taking into considerations plane reflections with that index), we find:

$$a = \frac{\lambda}{\sqrt{3}sin\theta}\sqrt{h^2 + k^2 + hk} \tag{26}$$

When h=k=0, the first term of 25 disappears and we can find a condition from which to obtain c:

$$c = \frac{\lambda l}{2sin\theta} \tag{27}$$

λ is still 1.5406 Å, while the lattice parameters according to our match sample are $a = b = 3.2427$ Å, $c = 5.1948$ Å. We will now plot the extrapolation functions to apply corrections to our lattice parameter.
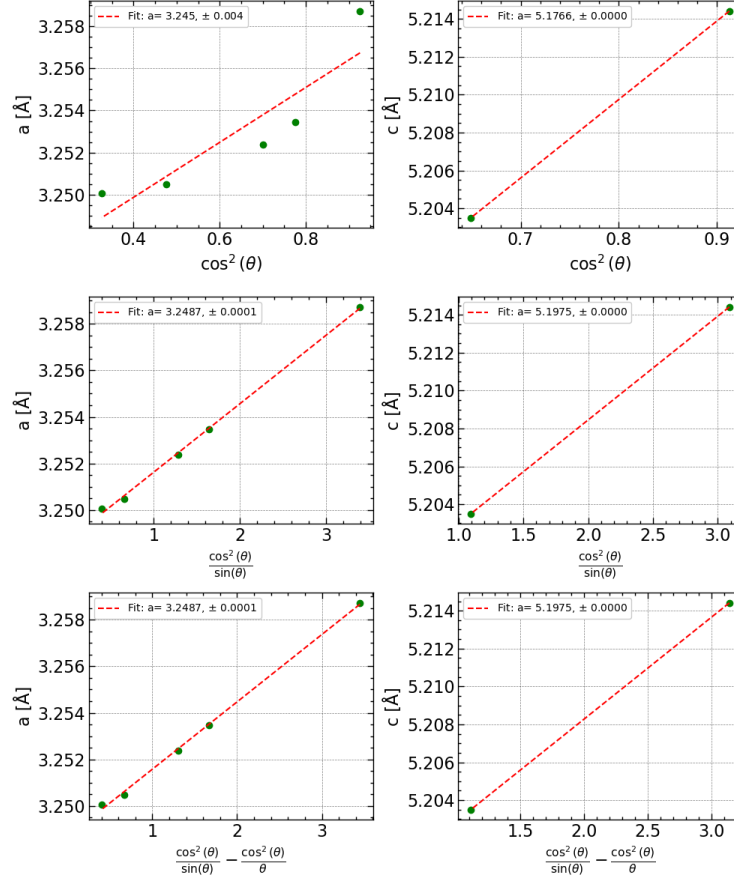
26

Figure 26: Extrapolation functions corrections of lattice parameter **a** (left) and **c** (right) for ZnO.

We see that the closest value for parameter **a** was obtained for the $\cos\theta^2$ extrapolation with **a**= 3.245 Å, presenting an error of only 0.07%. This could hint at potential absorption within the sample. As only two values are available for **c**, a further analysis wasn't conducted. Although, Nelson-Riley and $cos^2\theta/sin\theta$ functions presented an error of 0.05% in both cases with $c = 5.1975$ Å.

3.2 Task 2

In this task we explore the XRD patterns of two different ZnO thin films (about $1\mu m$ thick) grown on single-crystalline sapphire substrates with different orientation of the substrate surface. Prior to the analysis, we explore the geometry of sapphire substrate.

Sapphire Substrate

Single crystal of aluminium oxide, α-Al$_2$O$_3$, has a stable corundum at high temperatures, called sapphire. The basis of the crystal are octahedrons with O^{2-} ions at the corners, and Al^{3+} ions in the center. It has a trigonal crystal

structure, but generally treated as a hexagonal crystal as shown in the figure below:
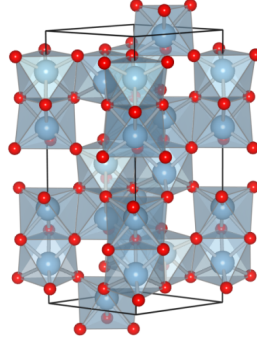

Figure 27: Corundum Structure of Sapphire (ICSD-10425; drawn using VESTA) [20]

By analysing the Miller indices of ZnO peaks, one can determine the growth direction of the thin film on the sapphire substrate. Different orientations of the substrate, such as the a-plane and r-plane, affect the growth mode, strain, and quality of the thin films. The a-plane $\{11\bar{2}0\}$ is perpendicular to the a-axis of the crystal, consisting of a hexagonal arrangement of oxygen atoms, exposing a nonpolar plane. The r-plane $\{1\bar{1}02\}$ is inclined relative to both the a-axis and c-axis, and consists of a mixture of Al and O atoms.
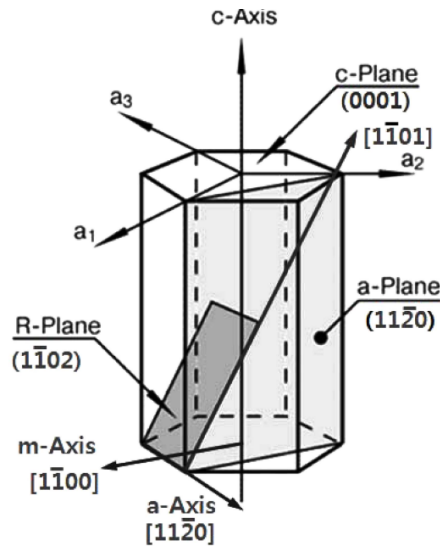

Figure 28: Axes and Planes of Sapphire Crystal [21]

3.2.1 ZnO on an a-plane oriented sapphire substrate

Position[°]	FWHM [°]	d-spacing [Å]	Rel. Int.[%]
31.0092	0.1181	2.88399	0.12
32.9332	0.0984	2.71978	0.09
34.4242	0.1181	2.60531	100.00
36.1657	0.2362	2.48375	0.02
37.7389	0.1574	2.38376	6.83
64.6654	0.1574	1.44145	0.00
72.5946	0.1440	1.30124	3.73
72.7929	0.1440	1.30140	1.87
80.6684	0.1200	1.19012	3.33
80.9137	0.1200	1.19008	1.93
122.7691	0.1440	0.87748	0.02
125.2815	0.2640	0.86731	0.94
125.8345	0.2640	0.86731	0.48

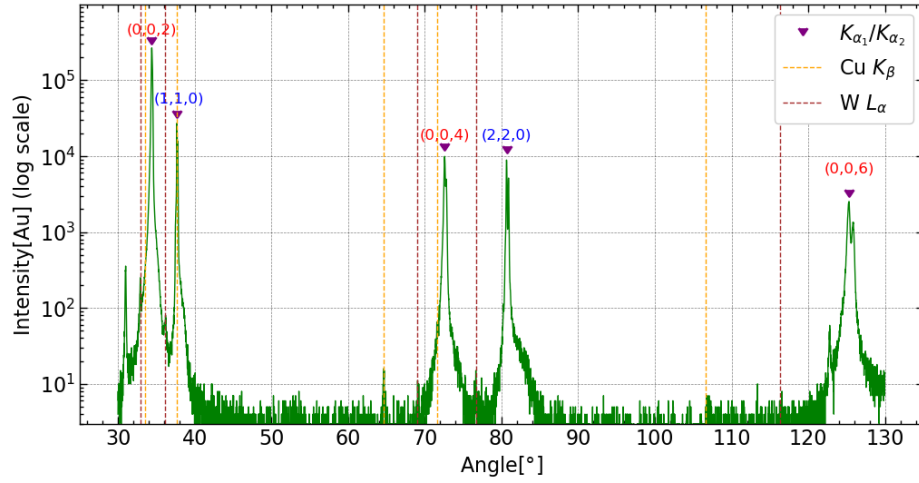Table 3: Position, FWHM, d-spacing and relative intensity for detected peaks.

Figure 29: Diffraction pattern of ZnO (red) on Al_2O_3 (blue) a-plane oriented with assigned Copper and Tungsten weak lines

The yellow and blue lines depict radiation from copper and tungsten respectively, as they get heated throughout the measurements. The identification of these lines were done via an in-built tool in the HighScore software.

In this and the following task, the indexing of sapphire lines was done by comparison to the data found in the appendix in [1], while the ZnO peaks were indexed in comparison to Figure 23.

We notice a reduction in the number of peaks compared to a powdered sample of ZnO. Bragg peaks from planes parallel to the sample surface are detected in comparison to the numerous orientations available in a powdered sample. A

higher count of intensity was also noted for the thin film, due to the lack of destructive interference between different indices.

The Bragg peaks obtained from the thin film, i.e. the (002), (004) and (006) planes are oriented parallel to the c-axis of ZnO wurtzite structure. Thus, the thin film has a preferential orientation along the c-axis, meaning that the c-axis of ZnO is perpendicular to the substrate surface. The growth direction of the ZnO thin film on a-plane sapphire is along the [0001] direction. The presence of higher order peaks (00l) depict good alignment likely due to the lack of polarization effects in the a-plane.

3.2.2 ZnO on an r-plane oriented sapphire substrate

Position[°]	FWHM [°]	d-spacing [Å]	Rel. Int.[%]
23,0890	0,0984	3,85220	0,15
24,4934	0,0984	3,63442	0,11
25,5984	0,1378	3,47997	100,00
34,3208	0,9446	2,61292	0,00
47,1772	0,0984	1,92654	0,15
50,2186	0,0984	1,81676	0,09
50,6685	0,1574	1,80168	0,04
52,5774	0,0984	1,74068	94,24
56,5671	0,1181	1,62701	4,35
73,7785	0,1574	1,28432	0,01
79,0512	0,1968	1,21136	0,00
82,8034	0,1440	1,16477	0,05
83,2544	0,1200	1,15960	4,85
83,5102	0,1200	1,15957	2,18
106,3397	0,1440	0,96237	0,02
116,1840	0,2400	0,90741	0,01
117,5902	0,3840	0,90060	0,00
123,8447	0,3360	0,87305	0,13
124,6922	0,1440	0,87180	19,09
125,2403	0,1440	0,86748	8,80

Table 4: Position, FWHM, d-spacing and relative intensity for detected peaks.
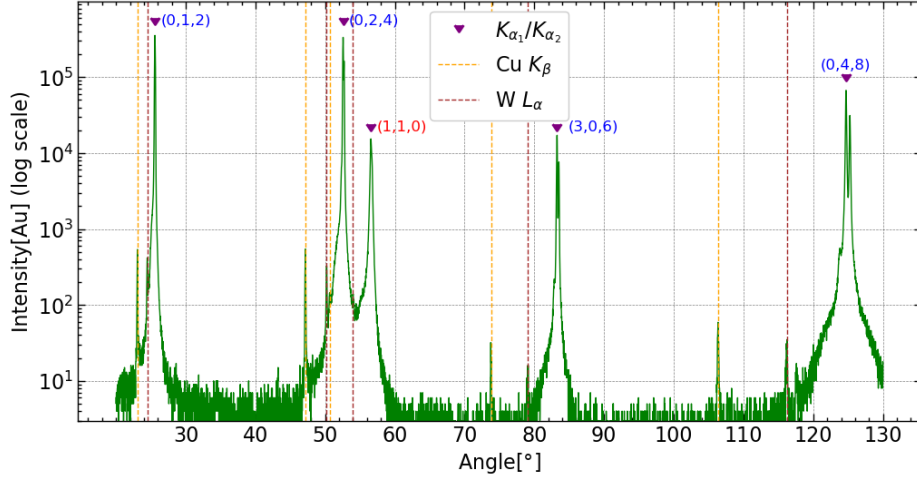
Figure 30: Diffraction pattern of ZnO (red) on Al_2O_3 (blue) r-plane oriented with assigned Copper and Tungsten weak lines

We notice, again, an even greater reduction of number of peaks of ZnO compared to the polycristalline sample. The Bragg peaks obtained from the thin film, i.e. the (110) plane, indicate that the a-axis ($[11\bar{2}0]$] direction) of ZnO is parallel to the surface of the r-plane sapphire. This implies that the c-axis of ZnO ([0001]] direction) is inclined relative to the substrate surface. In the case of r-plane sapphire, this means that thin film c-axis is tilted at an angle to the substrate surface plane, not perpendicular as with a-plane sapphire. This tilt can lead to unique strain and defect characteristics which we will analyse in the following section.

3.2.3 Rocking curves of selected peaks

Upon selection of the peak with the highest 2θ value for both substrate and thin film, we perform an ω-scan to determine FWHM of the rocking curves. It serves as an important and widely used structural quality criterion of textured epitaxial thin films and crystals. We present the two selected peaks for thin film grown on a-plane sapphire below:
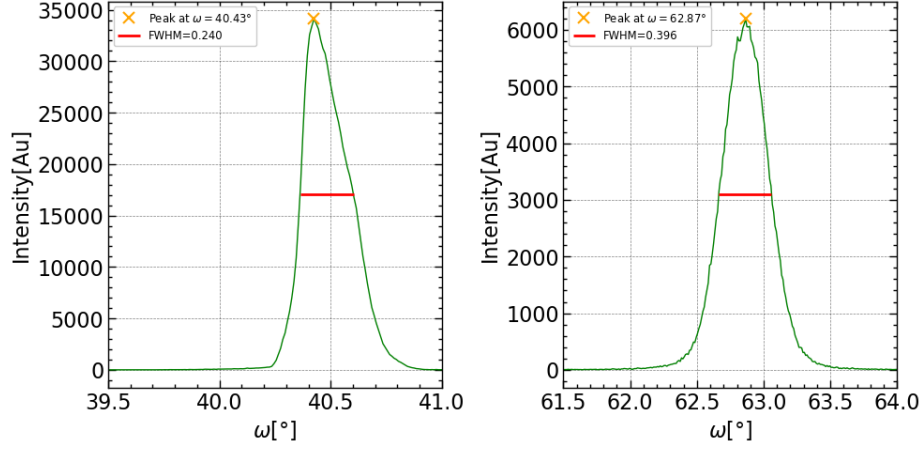
Figure 31: For a-plane: (220) Sapphire (left) and (006) ZnO (right)

The ω-scans were performed for the following:

Selected Peak	2θ [°]	FWHM 2θ[°]	FWHM ω[°]
(220) Sapphire	80.6684	0.1200	0.2400
(006) ZnO	125.2815	0.2640	0.396

Table 5: FWHM from a-plane sapphire ω-scan

As discussed in Section 1.11, crystallites form ensembles due to their angular tilt distribution with respect to the [0001] direction. In an ω-scan, these tilts induce a variation in the $2\theta - \omega$ peaks. This causes an increase in the angular FWHM of the peaks as can be seen from Table 5. The FWHM of the thin-film is around 40% larger than the one from the substrate. As the thin-film is epitaxied, it adapts to the lattice mismatch between the film and substrate that leads to dislocations in the crystal of the thin-film. The low FWHM of $2\theta - \omega$ peak of the thin-film also suggests that our sample size is large enough for sufficient destructive interference around the peak.

We also calculate the out-of-plane lattice constant using the K_{α_1} peak position of $2\theta = 125.2815°$, and $\lambda = 1.5406$Å along with equation (27) which yields **c=5.2039Å**. The theoretical match from PC-PDF of ZnO was found to be $c = 5.1948$Å, and our experimental result in Task 1 was $c = 5.1975$ Å. We have a slight deviation of about 0.1% from Task 1 parameter.

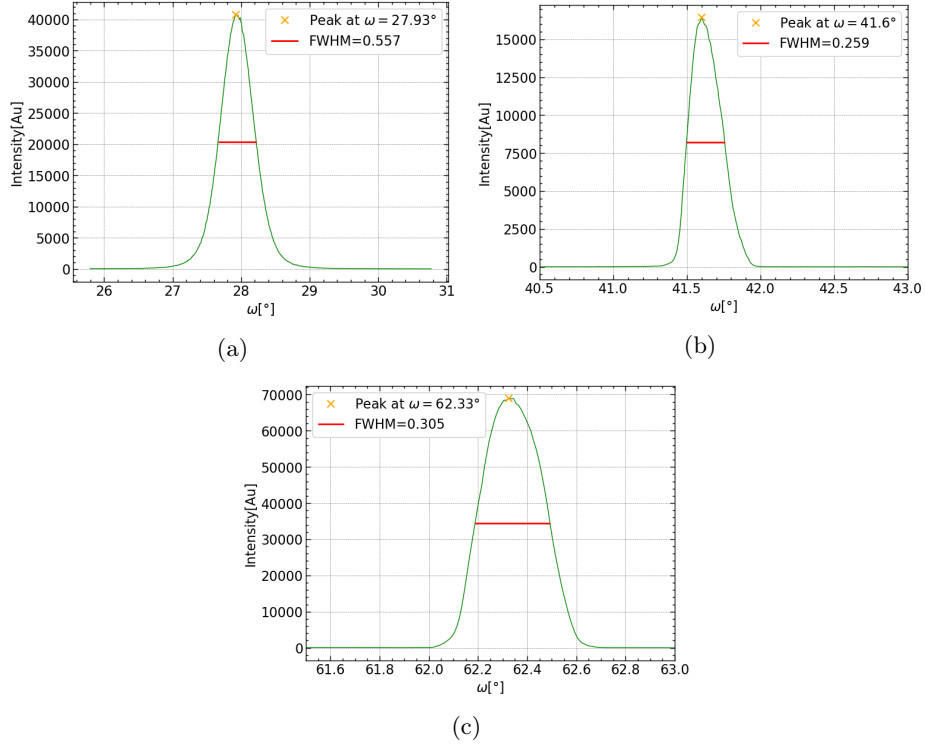We now compare the a-plane ω-scans with the r-plane sapphire.

Figure 32: For r-plane: (a) (110) ZnO (b) (306) Sapphire (c) (048) Sapphire

Due to initial uncertainty in the identity of the (048) Sapphire peak (c), we also performed the ω-scan for (306) Sapphire. The data obtained is also displayed below:

Selected Peak	2θ [°]	FWHM 2θ[°]	FWHM ω[°]
(110) ZnO	56.5671	0.1181	0.5570
(306) Sapphire	83.2544	0.1200	0.2590
(048) Sapphire	124.6922	0.1440	0.305

Table 6: FWHM from r-plane sapphire ω-scan

We see a significant increase in FWHM for the r-plane sapphire as well. For the (110) ZnO peak, the increase in ω width is almost 5 times that of the 2θ width. Such a drastic change in FWHM compared to the one seen in a-plane, suggests that the lattice-mismatch for r-plane is significantly higher.

We also calculate the out-of-plane lattice constant using the K_{α_1} peaks as done for the a-plane. Using (110) ZnO we find that **a=3.2513Å**. The theoretical match from PC-PDF of ZnO was found to be $a = 3.2427$Å, and our experimental result in Task 1 was $a = 3.245$ Å. We have a deviation of about 0.2% for (110), which is consistent with the finding of differently oriented sapphire.

Note that due to us measuring lattice planes parallel to sample surface, we are able to determine only out-of-plane parameters and tilt mosaicity. If lattice planes not parallel to sample surface were measured, we could have determined

in-plane properties and twist mosaicity. The ensemble-like nature of tilt and twist mosaicity is depicted below:
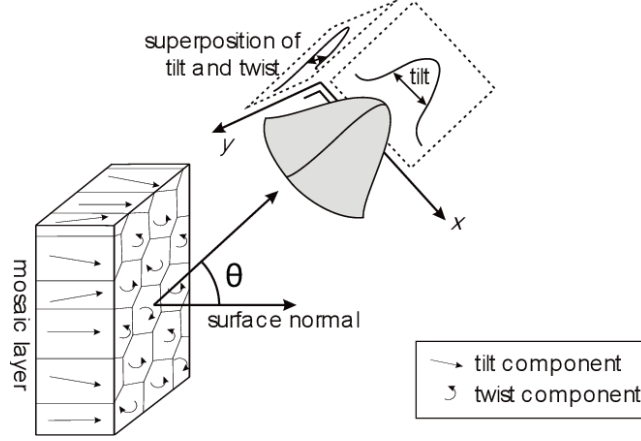

Figure 33: Twist and Tilt Mosaicity forming ensemble-like regions [23]

3.3 Task 3

In this task, we analyze an unknown sample of oxide powder (lab label: 2).
The diffraction pattern obtained is depicted below:
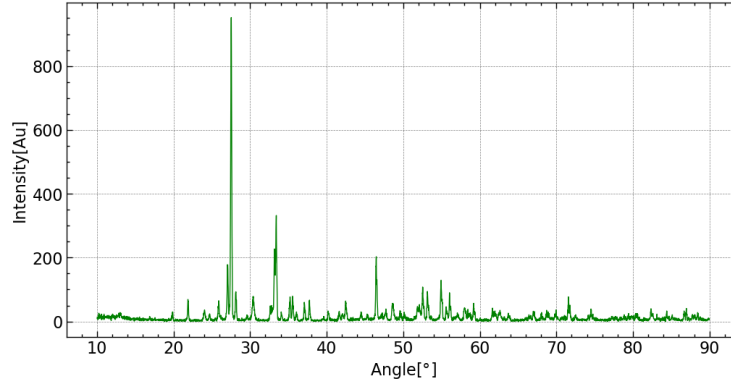
Figure 34: Diffraction pattern of an unknown powder sample.

As opposed to anisotropic thin films on substrates, every possible crystalline orientation is represented equally in a powder sample. As such we use the High X'Pert software to match our sample using the in-built match finder. The foremost importance is the position of the most intense peak, which is found at $2\theta = 27.54°$ or $\theta = 13.77°$. The highest intensity peak provides critical information about the planes that are most densely packed, which is vital for understanding the crystal structure.

$$Bi_2O_3 \qquad\qquad BaBi_{0.25}O_3Pb_{0.75}$$

$$Cu_{39}Sn_{11}$$

Figure 35: Powder diffraction of three best matches in order of similarity to our sample
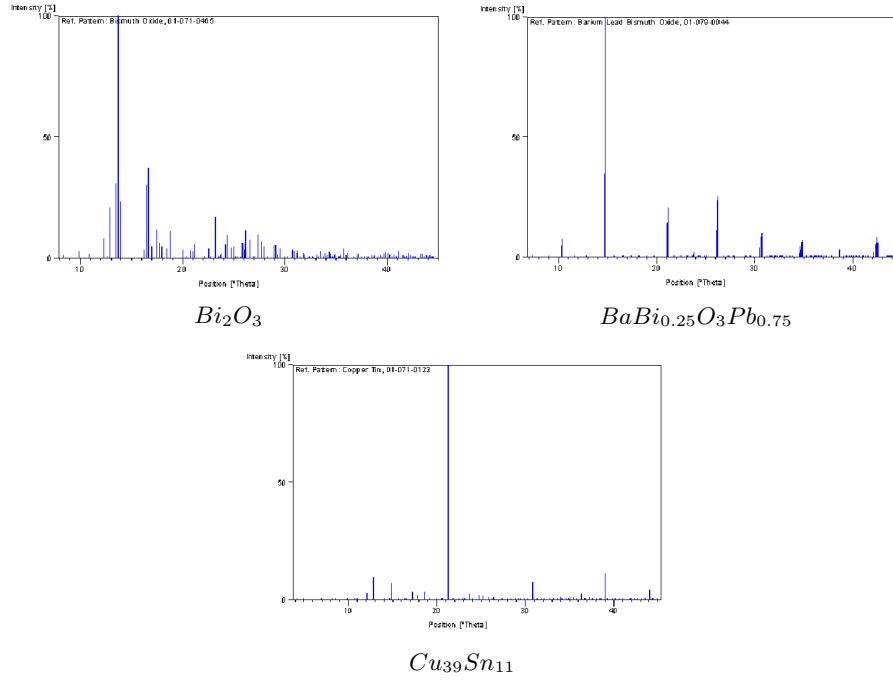
For the three matches, the most intense peak is found at:

Sample	Position of maximum peak$(2\theta)[°]$	Relative error to sample [%]
Bi_2O_3	27,392	0.54
$BaBi_{0.25}O_3Pb_{0.75}$	29,604	7.5
$Cu_{39}Sn_{11}$	42,557	54.5

We can conclude that the unknown powder's crystal structure is closest to our first match, Bismuth Oxide.

Bi_2O_3 presents a **monoclinic** primitive unit cell, thus having $a \neq b \neq c$ and $\alpha = \gamma = 90°$, $\beta \neq 90°$, hence the d-spacing will be given by (from appendix A):

$$\frac{1}{d_{hkl}^2} = \frac{h^2}{a^2 \sin^2 \beta} + \frac{k^2}{b^2} + \frac{l^2}{c^2 \sin^2 \beta} - \frac{2hl \cos \beta}{ac \sin^2 \beta} \qquad (28)$$

Further analysis and comparison of the lattice parameters of our sample with its match would be possible by once again indexing each peak and rewriting the former equation's with respect to Bragg's law. Due to the presence of 4 unknown parameters(a, b, c, β), as opposed to cubic and hexagonal systems having respectively only 1 and 2, it would not be a trivial exercise and goes beyond the scope of this report. Furthermore, the second best match $BaBi_{0.25}O_3Pb_{0.75}$ is chemically very different from bismuth oxide. XRD is an appropriate tool to perform structural analysis of samples, however it lacks the means to determine exact chemical composition.

4 Conclusion & Outlook

In task 1 we measured the diffraction patterns of two polycrystalline bulk samples Si and ZnO, and by peak indexing and error analysis we were able to estimate lattice parameters with a relative error in relation to the theoretical expected values of 0.04% for Silicon, and 0.07%, 0.05% (a and c) for ZnO. It is worth noting that, the manually indexed planes resulted in single worst estimation of lattice parameters, but consistently gave better estimation when included in the fits.

ZnO was further analyzed in Task 2, where we observed the loss of most of the peaks of its isotropic configuration when epitaxied as a thin film on a specifically oriented substrate (a-plane and r-plane sapphire). The only ZnO reflection planes we were able to resolve in the diffraction spectra were (0,0,2l) for a-plane sapphire, and (h,k,0) for r-plane sapphire. Additionally, an analysis of the ω angles for the peaks with the highest 2θ angle was carried forward, giving us insights on the extent of lattice mismatch between the two substances as described in Section 1.11. We also observe that the lattice parameters change in the context of thin films for ZnO is only minor: 0.2% for a and 0.1% for c.

Lastly in Task 3, we successfully identified structural similarity of an unknown powder sample to Bismuth Oxide. We emphasized the importance of XRD in determining crystal structure but not chemical composition.

References

[1] Michael Lorenz, *XRD - Analysis of structure of powder samples and epitaxial thin films.* University of Leipzig. Advanced laboratory exoeriment guide.

[2] Birkholz, Mario. (2014). Principles of X-ray Diffraction.

[3] Jan Drenth. (2007). *Principles of Protein X-Ray Crystallography.* Springers

[4] B. D. Cullity; S. R. Stock. (2013). *Elements of X-Ray Diffraction, third edition.* Pearson

[5] Klug, H. P.; Alexander, L. E. (1974). *X-Ray diffraction procedures: for polycrystalline and amorphous materials (2nd ed.).* John Wiley and Sons

[6] Seely, John & Pereira, Nino & Weber, Bruce & Schumer, Joseph & Apruzese, John & Hudson, Lawrence & Szabo, Csilla & Boyer, Craig & Skirlo, Scott. (2010). *Spatial resolution of a hard x-ray CCD detector.* Applied optics. 49. 4372-8. 10.1364/AO.49.004372.

[7] Zhang Y; Evans JRG and Zhang S (January 2011). "Corrected Values for Boiling Points and Enthalpies of Vaporization of Elements in Handbooks". J. Chem. Eng. Data. 56 (2): 328–337. doi:10.1021/je1011086.

[8] Simon S. H. (January 9, 2012)Lecture Notes for Solid State Physics (3rd Year Course 6) Hilary Term 2012, Oxford University

[9] Ashcroft, N. W., Mermin, N. D. (1976). Solid State Physics. Holt-Saunders.

[10] L. Spieß et al. Moderne Rontgenbeugung: Röntgendiffraktometrie für Materialwissenschaftler, Physiker und Chemiker. Springer Fachmedien Wiesbaden, 2019. ISBN: 9783834882325

[11] Alkhatab, Mohammad. (2020). Material studies for flexible 3rd generation solar cells.

[12] Bourget. L. et al. MKS Instruments Handbook: Semiconductor Devices & Process Technology (2023)

[13] Grundmann, M. (2016). The Physics of Semiconductors. Springer

[14] Fleck. M. (2020). An illustration of the burgers vector. Wikimedia (URL:https://commons.wikimedia.org/wiki/File:Burgers_Vector_and_dislocations_(screw_and_edge_type).svg)

[15] Speakman, S. (2014). Introduction to High Resolution XRD of Epitaxial Thin Films. MIT Center for Materials Science and Engineering

[16] Rajendrachari, Shashanka & Swamy, Kumara. (2020). Biosynthesis of Silver Nanoparticles Using Leaves of Acacia Melanoxylon and their Application as Dopamine and Hydrogen Peroxide Sensors. Physical Chemistry Research. 8. 1-18. 10.22036/pcr.2019.205211.1688.

[17] Árnason, Hákon. (2018). Silicon nanowires - Photovoltaic and thermoelectric applications.

[18] Zinc Oxide: Fundamentals, Materials and Device Technology. Hadis Morkoç and Ümit ÖzgurCopyright Ó 2009 WILEY-VCH Verlag GmbH & Co. KGaA, Weinheim ISBN: 978-3-527-40813-9

[19] Kumar, R., Al-Dossary, O., Kumar, G. et al. Zinc Oxide Nanostructures for NO2 Gas–Sensor Applications: A Review. Nano-Micro Lett. 7, 97–120 (2015). https://doi.org/10.1007/s40820-014-0023-3

[20] Crystallography matters...more! (2014), Crystallography365 (URL:https://www.iycr2014.org/learn/crystallography365/categories/inorganic-structures?result_105899_result_page=37)

[21] Kang, Jin-Ki & Kim, Jung & Kim, Young-Jin. (2011). Fabrication of R-plane Sapphire wafer for Nonpolar a-plane GaN. Journal of the Microelectronics and Packaging Society. 18.

[22] Golubovic, Aleksandar & Nikolic, Sanja & Đurić, S. & Valčić, A.. (2001). The Growth of Sapphire Single Crystals. Journal of the Serbian Chemical Society. 66. 411-418.

[23] Vries, B.L., Wahl, U., Ruffenach, S., Briot, O., & Vantomme, A. (2013). Influence of crystal mosaicity on axial channeling effects and lattice site determination of impurities. Applied Physics Letters, 103, 172108.

Appendix A   Crystal Systems and their d-spacing

Cubic:
$$a = b = c, \quad \alpha = \beta = \gamma = 90°$$
$$\frac{1}{d_{hkl}^2} = \frac{h^2 + k^2 + l^2}{a^2}$$

Tetragonal:
$$a = b \neq c, \quad \alpha = \beta = \gamma = 90°$$
$$\frac{1}{d_{hkl}^2} = \frac{h^2 + k^2}{a^2} + \frac{l^2}{c^2}$$

Hexagonal:
$$a = b \neq c, \quad \alpha = \beta = 90°, \quad \gamma = 120°$$
$$\frac{1}{d_{hkl}^2} = \frac{4}{3}\left(\frac{h^2 + k^2 + hk}{a^2}\right) + \frac{l^2}{c^2}$$

Rhombohedral:
$$a = b = c, \quad \alpha = \beta = \gamma \neq 90°$$
$$\frac{1}{d_{hkl}^2} = \frac{(h^2 + k^2 + l^2)\sin^2\alpha + 2(hk + kl + hl)\cos^2\alpha - \cos\alpha}{a^2(1 - 3\cos^2\alpha + 2\cos^3\alpha)}$$

Orthorhombic:
$$a \neq b \neq c, \quad \alpha = \beta = \gamma = 90°$$
$$\frac{1}{d_{hkl}^2} = \frac{h^2}{a^2} + \frac{k^2}{b^2} + \frac{l^2}{c^2}$$

Monoclinic:
$$a \neq b \neq c, \quad \alpha = \gamma = 90°, \beta \neq 90°$$
$$\frac{1}{d_{hkl}^2} = \frac{h^2}{a^2 \sin^2\beta} + \frac{k^2}{b^2} + \frac{l^2}{c^2 \sin^2\beta} - \frac{2hl\cos\beta}{ac \sin^2\beta}$$

Triclinic:
$$a \neq b \neq c, \quad \alpha \neq \beta \neq \gamma \neq 90°$$
$$\frac{1}{d_{hkl}^2} = \frac{1}{V^2}\left(S_{11}h^2 + S_{22}k^2 + S_{33}l^2 + 2S_{12}hk + 2S_{23}kl + 2S_{13}hl\right)$$

The coefficients for triclinic crystals are given by $S_{11} = b^2c^2 \sin^2\alpha$, $S_{22} = a^2c^2 \sin^2\beta$, $S_{33} = a^2b^2 \sin^2\gamma$, $S_{12} = abc^2(\cos\alpha\cos\beta - \cos\gamma)$, $S_{23} = a^2bc(\cos\beta\cos\gamma - \cos\alpha)$, and $S_{13} = ab^2c(\cos\gamma\cos\alpha - \cos\beta)$, with V being the volume of the unit cell [4].